



Comparison of Electrochemical Properties of La_{0.6}Sr_{0.4}FeO_{3-δ} Thin Film Electrodes: Oxidizing vs. Reducing Conditions

Sandra Kogler, Andreas Nenning, Ghislain M. Rupp, Alexander K. Opitz, and Jürgen Fleig^{*,z}

Institute of Chemical Technologies and Analytics, Vienna University of Technology, 1060 Vienna, Austria

Owing to its mixed ionic and electronic conductivity and high thermochemical stability, La_{0.6}Sr_{0.4}FeO_{3-δ} (LSF64) is an attractive electrode material in solid oxide fuel/electrolysis cells (SOFCs/SOECs). Well defined thin film microelectrodes are used to compare the electrochemical properties of LSF64 in oxidizing and reducing conditions. The high electronic sheet resistance in hydrogen can be overcome by the use of an additional metallic current collector. With the sheet resistance being compensated, the area specific electrode resistance is similar in humidified hydrogen and oxygen containing atmospheres. Analysis of the chemical capacitance and the electrode resistance for current collectors on top and beneath the LSF64 thin film allow mechanistic conclusions on active zones and bulk defect chemistry. Cyclic gas changes between reducing and oxidizing conditions, performed on macroscopic LSF64 thin film electrodes with top current collector, reveal a strong degradation of the surface kinetics in synthetic air with very fast recovery in reducing atmosphere. Additional in-situ high-temperature powder XRD on LSF64 demonstrates the formation of small amounts of iron oxides in humidified hydrogen at elevated temperatures.

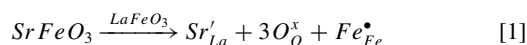
© The Author(s) 2015. Published by ECS. This is an open access article distributed under the terms of the Creative Commons Attribution Non-Commercial No Derivatives 4.0 License (CC BY-NC-ND, <http://creativecommons.org/licenses/by-nc-nd/4.0/>), which permits non-commercial reuse, distribution, and reproduction in any medium, provided the original work is not changed in any way and is properly cited. For permission for commercial reuse, please email: oa@electrochem.org. [DOI: 10.1149/2.0731503jes] All rights reserved.

Manuscript submitted September 29, 2014; revised manuscript received December 23, 2014. Published January 6, 2015.

Solid oxide fuel cells (SOFCs) are in the process of gaining more and more commercial success as highly efficient power generation systems. They transform the chemically bound energy of a fuel to electrical energy. Solid oxide electrolysis cells (SOECs) are the counter parts of SOFCs as they use electrical energy, e.g. excess energy from the grid, to form fuel by electrolysis. Owing to their very high efficiencies, also SOECs are promising devices in future energy technologies.¹ Currently Ni/YSZ cermet electrodes are the standard electrodes in SOF/ECs for reducing conditions, but they are known to suffer from several problems, like sulfur poisoning (in SOFC operation), sintering, redox cycle stability etc.² To find an alternative to Ni/YSZ could therefore be favorable for both SOFCs and SOECs.

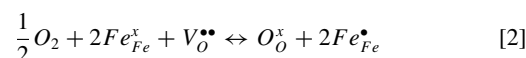
Electrodes in SOE/FCs have to meet numerous requirements: thermochemical stability over a wide oxygen partial pressure range, high catalytic activity for oxygen exchange reactions, compatibility with adjacent cell components, sufficiently high electronic and ionic conductivity, etc. Perovskite-type oxides such as LaMnO₃, LaCoO₃ and LaFeO₃ based materials are used in state-of-the-art SOF/EC electrodes in oxygen atmosphere. Often they are mixed ionic and electronic conductors (MIECs), which is advantageous in SOF/ECs as the whole electrode surface area may become active in the oxygen exchange reaction. Employing such MIECs also in reducing atmosphere could be highly attractive. However, Sr-doped LaMnO₃ and LaCoO₃ are only stable under comparatively high oxygen partial pressures and thus not suited for the use in hydrogen.³⁻⁵ Therefore, generally other compositions such as (La,Sr)(Cr,Mn)O₃,⁶⁻⁹ (La,Sr)(Cr,V)O₃,^{10,11} (La,Sr)(Cr,Ru)O₃,^{12,13} or La and Fe doped SrTiO₃^{14,15} are tested under reducing conditions.¹⁶

Although Sr-doped LaFeO_{3-δ} (LSF) is a typical SOFC cathode material, it is also rather stable in reducing conditions,¹⁷⁻¹⁹ with La_{0.6}Sr_{0.4}FeO_{3-δ} decomposing below 10⁻²⁷ bar pO₂ at 600°C.¹⁹ Moreover, its thermal expansion coefficient matches acceptably well with typical electrolytes in SOF/ECs.^{19,20} Several studies were performed on the defect chemistry and transport properties of LSF²¹⁻³¹ and lead to the following defect chemical picture: Substitution of La³⁺ by Sr²⁺ acts as acceptor doping and causes both a partial valence change of iron from Fe³⁺ to Fe⁴⁺ and the formation of oxygen vacancies.^{19,32} In Kröger-Vink notation this is written as



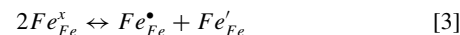
*Electrochemical Society Active Member.

^zE-mail: juergen.fleig@tuwien.ac.at



Fe⁴⁺ states can be interpreted as electron holes (h^{*}) and those determine the electronic conductivity at high oxygen partial pressure as they are the majority mobile charge carrier.²⁰⁻²²

Towards lower oxygen partial pressures (and/or higher temperatures) the equilibrium of Eq. 2 is shifted to the left hand side, increasing the amount of oxygen vacancies and thus the ionic conductivity.^{23,24} Concurrently, oxygen release causes a reduction of the iron, which decreases the concentration of electron holes. This also increases the electron concentration (i.e. Fe²⁺)¹⁹ in accordance with



In humidified hydrogen Fe'_{Fe} becomes the predominant electronic charge carrier. Besides concentration and type of electronic charge carriers, also their mobility is affected by the higher amount of oxygen vacancies. Since the electronic transfer occurs along Fe-O-Fe chains, a disruption of these chains by oxygen vacancies hinders the hopping of the electronic charge carriers.^{25,33-35} As a result, in reducing atmospheres the electronic conductivity is much smaller than in air.²

The decreased electronic conductivity of LSF and other acceptor doped perovskite-type oxides in reducing atmosphere can be a problem for their use as electrode materials as it causes resistive losses from the outer current collector to the reaction site. However, the lack of electronic conductivity could be compensated by additional current collectors. In analogy to Ni/YSZ, where YSZ supplies the ionic conductivity, a metal may be used in combination with an acceptor-doped oxide such as LSF to provide sufficient electronic conductivity in a composite electrode.

This approach of applying a cermet with an electrochemically active mixed conducting oxide and a current collecting metal is much less common than composites of MIECs with a pure ion conductor. A realization with ceria-based thin films and metal current collectors can be found in Ref. 36 and an in-situ XPS study of electrochemically active zones in ceria films with gold current collectors was presented in Ref. 37. Also, in a recent study on Sr(Ti,Fe)O₃ in H₂/H₂O, such thin film model composites were employed.³⁸ A novel electrode geometry with two interdigital Pt current collectors within a single microelectrode allowed detailed mechanistic conclusions on the kinetic losses from electronic and ionic charge transport and the H₂ oxidation/H₂O splitting reaction on such electrodes. The impedance response of mixed conducting thin film electrodes with well-defined patterned

metal current collectors in a symmetrical cell was also numerically modeled.³⁹ Those studies revealed that such model type experiments based on MIEC thin films and current collectors are highly valuable in order to better understand properties and limitations of mixed conducting SOFC anodes/SOEC cathodes. However, mechanistic studies on LSF thin film electrodes in H_2/H_2O are rare, one study reports its performance in a SOEC cell.⁴⁰ A systematic investigation of its electrochemical properties in reducing conditions and a comparison with those in air is still missing.

In the present study, we therefore investigate the effect of humidified H_2 and gas changes between reducing and oxidizing conditions on the electrochemical properties of $La_{0.6}Sr_{0.4}FeO_{3-\delta}$ (LSF64) thin films on yttria stabilized zirconia (YSZ) electrolytes. Impedance spectroscopy was used to analyze the resistance related to the surface reaction kinetics and the chemical capacitance of thin film microelectrodes with and without a micro-patterned current collector. Additional measurements on macroscopic LSF64 thin films showed the impact of cyclic gas changes on the polarization resistance and the associated chemical capacitance. In-situ high-temperature XRD diffraction patterns, recorded under humidified H_2 at elevated temperatures, revealed information on the phase stability.

Experimental

LSF64 powder was synthesized by Pecchini's⁴¹ method: Fe_2O_3 (99.99% Alfa Aesar), $SrCO_3$ ($\geq 99.99\%$ Aldrich) and La_2O_3 ($\geq 99.99\%$ Sigma-Aldrich) were weighed according to the desired stoichiometry, the compounds were dissolved in HNO_3 (65% extra pure, Merck). Citric acid ($\geq 99.9998\%$ Fluka) was added to the solution with 1:1.1 molar-ratio of cations. The solution was concentrated to form a gel. The gel was further heated until self-ignition took place. The attained powder was calcined for 3 h at $900^\circ C$ and then annealed for 5 h at $1200^\circ C$. After calcination the powder was grinded and pressed into a pellet using a cold isostatic press. The pellet was then sintered at $1250^\circ C$ for 5 h. Phase purity was confirmed by powder X-ray diffraction (XRD) (Philips X'Pert).

The LSF64 pellet was used as target for pulsed laser deposition (PLD). (100) oriented single crystals of yttria stabilized zirconia (YSZ) (9.5 mol% Y_2O_3 , Crystec Germany) were employed as substrate. Ablation was done by a KrF excimer laser (Compex Pro 201 F) with 248 nm wavelength and an intensity of 400 mJ/pulse for 30 min

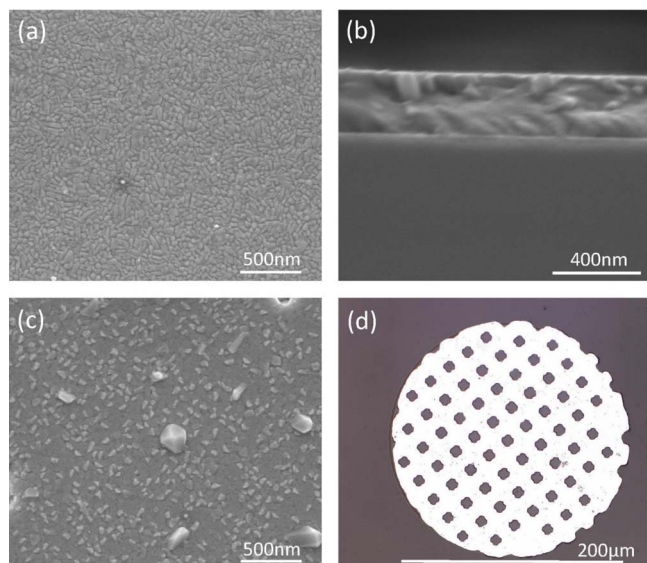


Figure 1. a) SEM image of a LSF64 thin film after PLD deposition on YSZ; b) breaking edge of a 420 nm thick LSF64 thin film; c) LSF64 thin film after heating in humidified hydrogen for 70 h at $T_{calc} = 622^\circ C$; d) a light microscope image of a LSF microelectrode with top current collector.

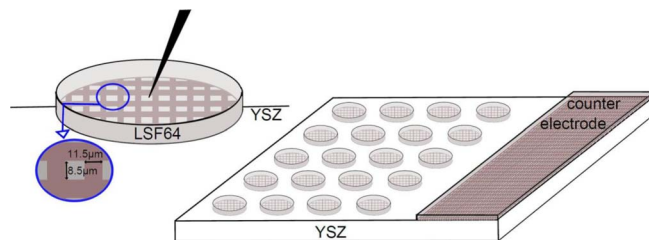


Figure 2. Left: sketch of a microelectrode with bottom current collector and zoom-in illustrating the current collector geometry; right: sketch of microelectrodes and a macroscopic counter electrode on a single crystalline substrate.

with 5 Hz pulse repetition rate for microelectrode samples and 45 min for macroelectrode samples. The distance between oxide target and substrate during ablation was 6 cm. The substrate temperature was approximately $650^\circ C$, measured by a Heitronics KT 19.99 pyrometer. The oxygen pressure was $4 \cdot 10^{-2}$ mbar within the PLD chamber. After deposition, the substrate with the thin film was cooled at a rate of $15^\circ C/min$. After deposition SEM pictures (FEI TECNAI F20) of the surface and a cross section of the thin film showed a pore-free and dense polycrystalline film of typically 200–400 nm thickness (see Fig. 1a and 1b). 220 nm and 330 nm thin films were used in the impedance measurements. After heating in humidified hydrogen for 70 h at $T_{calc} = 622^\circ C$ the thin films are still dense, however small crystallites grow on top of the thin film (see Fig. 1c).

For current collection titanium (BAL-TEC) (15 nm) and platinum (99.95% pure, ÖGUSSA) (100 nm) films were sputter deposited (MED 020 Coating System, BAL-TEC, Germany), with the titanium acting as adhesion layer. The sputter current was 100 mA, with the distance between sample and target being 6 cm. The argon pressure was set to $7 \cdot 10^{-3}$ (Ti) and $2 \cdot 10^{-2}$ mbar (Pt), yielding a sputter rate of 0.18 nm/sec (Ti) and 0.75 nm/sec (Pt), respectively.

Two types of samples were prepared: Circular LSF64 microelectrodes (95 and 195 μm diameter, 220 nm thickness) with current collector on top (see Fig. 1d) or beneath (8.5 μm distance between stripes of 11.5 μm width, see Fig. 2) and macroscopic LSF64 electrodes ($5 \times 5 mm^2$, 330 nm thickness) with current collecting fingers on top (Fig. 3). For the microelectrodes (Fig. 2) micro-patterning of the LSF64 thin film including current collector was carried out by standard photolithography and Ar ion-beam etching (tectura GmbH, ionEtch Sputter Gun). An approximately $1.5 \times 5 mm^2$ sized LSF64 thin film stripe with current collector was used as the counter electrode (CE) in impedance measurements. Additionally, for contacting reasons, platinum paste was brushed onto the back side of these samples and connected to the CE stripe. Owing to its much bigger size compared to the microelectrodes the contribution of the CE to the impedance spectrum can safely be assumed to be negligible.⁴²

In case of the macroscopic samples (Fig. 3), porous LSF64 with platinum paste on top was deposited on the back side of the YSZ single crystal and used as counter electrode. The polarization resistance of such a counter electrode was additionally measured in a conventional macroscopic setup on a symmetrical YSZ sample with two extended porous LSF64 electrodes. A value of ca. $1.1 \Omega cm^2$ in air and $1.5 \Omega cm^2$ in reducing conditions was found at $683^\circ C$. This is

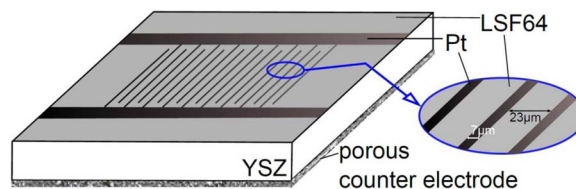


Figure 3. Sketch of a macroscopic electrode with metallic fingers on top and a porous counter electrode on the back side, also a zoom-in with geometric dimensions of the metallic fingers is shown.

significantly smaller than the polarization resistance of the macroscopic LSF64 thin film electrode ($>6 \Omega\text{cm}^2$) but is still visible in the impedance spectra (see section Results and Discussion). It can be identified by the relaxation frequency which differs from that of the thin film electrode.

For electrochemical measurements on microelectrodes, the samples were placed on a heating stage (Linkam, UK) in a vacuum chamber.⁴³ Impedance measurements were carried out under ambient or synthetic air (indicated for each measurement) and $\text{H}_2/\text{H}_2\text{O}/\text{Ar}$. Humidification of the 2.5% H_2/Ar (Air liquide, ARCAL 10) gas was achieved by slowly bubbling the gas through distilled water at room temperature. The resulting partial pressure of H_2O in the gas was assumed to be equal to the vapor pressure of saturated water at ca. 22°C (~ 26 mbar). The electrodes were contacted using Pt/Ir alloy needles with a typical tip radius of 3–8 μm . Contact needles were accurately positioned by micromanipulators (Karl Suss) under an optical microscope. Impedance measurements on macroscopic electrodes were carried out in a tube furnace (Gero, SR 40-200/12) under synthetic air and humidified $\text{H}_2/\text{H}_2\text{O}/\text{Ar}$ (see above). Sample contacting was achieved by Pt wires.

Impedance spectra on both sample types were measured in a frequency range of 10^6 to 10^{-1} or 10^{-2} Hz with an rms of 10 mV (Alpha A impedance analyzer, Novocontrol). In case of macroscopic samples the temperature was measured by a thermocouple close to the sample. In microelectrode measurements⁴³ the asymmetric heating and the local cooling by the contact tip cause a substantial deviation of true electrode temperatures from set temperatures. A reasonable estimate (T_{calc}) of the true electrode temperature can be obtained from the measured YSZ electrolyte resistance if electrode geometry and the YSZ conductivity vs. temperature are known.⁴⁴ Here, approximately 610°C–625°C are found for a set temperature of 700°C.

Diffraction patterns were recorded using Cu-K α radiation, with 0.008° steps and 3 hour dwell from 20° to 80° 2 θ (PANalytical, X'Pert Pro). The powder (approximately 1 g) was placed in the XRK 900 reaction chamber (Anton Paar) which allows high-temperature in-situ X-ray diffraction. In the chamber the powder was placed on a frit with a flux of humidified hydrogen (same as for impedance measurements). The gas flow was already applied 1 h before starting the measurement. A total of 29 XRD diffraction patterns in 2 θ scan geometry was measured while heating the powder to the maximum temperature of 800°C and cooling it down again in multiple steps. A full 2 θ scan (20°–80°, step size 0.008°, PANalytical, X'Pert Pro) was collected at each step for 1 h or 3 h (at 50°C, 800°C, 50°C). The long dwell time and the small angular steps increased sensitivity to compensate the high background of the Fe containing samples. Peaks were compared to ICDD-database: 01-082-1961 for LSF64 ($\text{La}_{0.6}\text{Sr}_{0.4}\text{FeO}_{2.796}$), 00-001-1111 for Magnetite (Fe_3O_4), 00-002-1180 for Wustite (FeO), 00-029-1305 for SrFeLaO_4 (A_2BO_4 , Ruddlesten Popper) and 00-057-0088 for $\text{LaSrFe}_2\text{O}_{5.5}$ ($\text{A}_2\text{B}_2\text{O}_{5.5}$, Brownmillerite).

Results and Discussion

Electrode impedance under dry oxidizing conditions.— Typical impedance spectra of LSF64 microelectrodes (195 μm diameter) with and without additional current collector, measured under ambient air at a set temperature of 700°C ($T_{\text{calc}} = 619^\circ\text{C}$), are shown in Fig. 4. The spectra exhibit a high frequency non-zero axis intercept, R_a . At intermediate frequencies, microelectrodes with additional current collector show a small depressed semicircle with resistance R_b , while microelectrodes without current collector only exhibit a slight shoulder, see inset of Fig. 4a. For both types of microelectrodes a dominant semicircle is observed at low frequencies with resistance R_c and capacitance C_c .

In accordance with literature,^{44–46} the high frequency axis intercept R_a is assigned to the ohmic resistance of the electrolyte (and used to calculate T_{calc}).⁴² At elevated temperatures, the electrolyte only causes an intercept instead of a semicircle due to its low capacitance.⁴⁵ R_a is almost identical for both types of microelectrodes, which indicates high in-plane electronic conductivity in air, see below and Ref. 47.

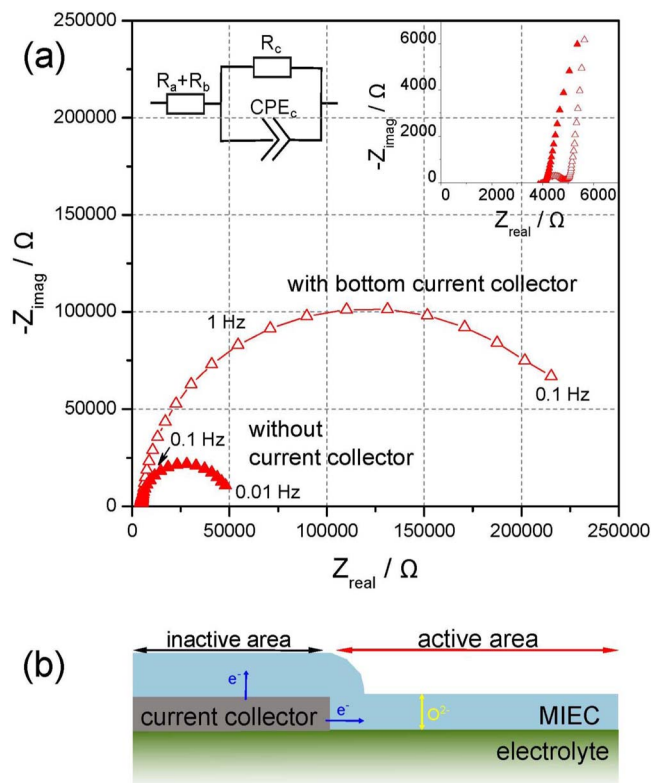


Figure 4. a) Impedance spectra of LSF64 microelectrodes (195 μm diameter) in ambient air, with bottom (open triangles) and without (filled triangles) current collector. The electrode temperature T_{calc} , calculated from the high frequency offset R_a , is 619°C for both measurements. Right inset: zoom of the high frequency range of the impedance spectra. Left inset: simple equivalent circuit, used to fit the low frequency arc in the impedance spectra. b) Schematic picture of active and inactive electrode surface areas for electrodes with (bottom) current collector.

According to literature,⁴⁵ the intermediate frequency feature is caused by the small interfacial resistance R_b between the LSF64 electrode and the YSZ electrolyte. Its capacitance C_b describes stoichiometric changes at the electrode/electrolyte interface and/or charging of the electrostatic double layer capacitance.⁴⁵ In case of the additional bottom current collector, the interfacial impedance is much more pronounced than for the microelectrode without current collector. This might be a simple consequence of geometry. The current collector covers approximately 80% of the electrode/electrolyte interface, therefore the interfacial resistance strongly increases. However, owing to its minor impact on the DC resistance, a more detailed analysis of this effect is beyond the scope of this paper. Also in the equivalent circuit used to parameterize the spectra, the intermediate frequency feature is only considered in terms of R_b while neglecting its capacitance (see Fig. 4). The main resistive process at low frequencies (R_c), reflected by the dominant second arc, is attributed to the oxygen exchange at the surface of the electrode.⁴⁵ In accordance with Ref. 45, the parallel capacitor (represented by CPE_c , see below) is caused by changes of the oxygen content in the electrode bulk (stoichiometry change) and is usually referred to as chemical capacitance.

This chemical capacitance C_{chem} can, with the assumption of diluted charge carriers and the absence of traps, be expressed by^{48,49}

$$C_{\text{chem}} = \frac{e^2}{kT} AL \left(\frac{1}{z_{\text{ion}}^2 c_{\text{ion}}^{\text{eq}}} + \frac{1}{z_{\text{eon}}^2 c_{\text{eon}}^{\text{eq}}} \right)^{-1} \quad [4]$$

with e denoting the elementary charge, k Boltzmann's constant, T temperature, z charge number ($z_{\text{ion}} = 2$, $z_{\text{eon}} = 1$) and c^{eq} the concentration of ionic and electronic charge carriers in equilibrium, respectively. In this paper, the chemical capacitance is mostly normalized to the MIEC

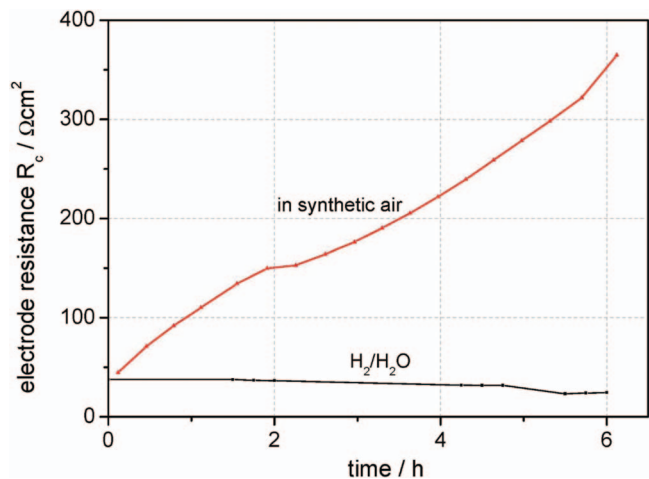


Figure 5. Electrode resistance per area over time for a strongly degrading circular microelectrode without current collector in synthetic air at $T_{\text{calc}} = 561^\circ\text{C}$ (red) and a circular microelectrode with top current collector (resistance normalized to free surface area) in humidified hydrogen at $T_{\text{calc}} = 616^\circ\text{C}$ (black).

volume involved, given by area A and film thickness L . According to Eq. 4, the minority charge carrier determines the chemical capacitance. In case of LSF64 in air, the minority charge carriers are oxygen vacancies, while electronic charge carriers should determine C_{chem} under reducing conditions.¹⁹ In the equivalent circuit, a constant phase element (CPE_c) is used instead of an ideal capacitance, accounting for non-ideal semicircles in the spectra. Its impedance Z_{CPE_c} is defined by

$$Z_{\text{CPE}_c} = \frac{1}{[T_c(j \cdot \omega)^{P_c}]^{1/P_c}} \quad [5]$$

with j and ω denoting imaginary unit and angular frequency, respectively. The relation

$$C_c = C_{\text{chem}} = (R_c^{1-P_c} \cdot T_c)^{\frac{1}{P_c}} \quad [6]$$

is used to calculate the corresponding capacitance, where P_c and T_c are fit parameters.⁵⁰

After the normalization to the entire film volume, the chemical capacitances of the spectra in Fig. 4 have values of 1293 F/cm³ and 289 F/cm³ for the sample without and with current collector, respectively. These values are in the order of magnitude expected for C_{chem} of MIEC thin film electrodes.⁵¹ The P_c values of 0.98 and 0.94 without and with current collector, respectively, show that the capacitor is almost ideal, as expected for a chemical capacitance. The area specific electrode resistance (ASR) in air, deduced from R_c and the total electrode area (A_{tot}), is 13.6 Ωcm² without current collector and 68.2 Ωcm² with current collector. These values are somewhat lower than those reported in Ref. 52 (200 Ωcm² at 610°C) possibly due to different deposition parameters or thermal history.

Several values of electrodes with and without current collector scale by similar factors: inverse ASR (0.2:1), chemical capacitance (0.22:1) and free electrode area without current collector (0.18:1). The ratio of the ASR should be taken with some caution since absolute values of ASR can be strongly affected by degradation, especially in the case of microelectrodes measured in the asymmetrically heated set-up.⁴³ As an example of a strong degradation process, Fig. 5 shows the increase of the main electrode polarization resistance R_c with time. Exact reasons for this fast degradation are unknown yet, but might be related to silicon poisoning⁵³ in the microcontact set-up. In absence of gas cycling such a fast degradation was not found in the experiments on macroscopic LSF64 thin film electrodes performed in a different set-up (see below). In this contribution only freshly prepared samples were considered and we therefore exclude degradation as major cause of

the measured resistance difference. The chemical capacitance is much less prone to time dependent changes and scatter between different electrodes.

Similarity of all these factors indicates that the MIEC volume above the current collector is not polarized and does neither contribute to oxygen exchange nor to the chemical capacitance (see Fig. 4b). This is not surprising taking into account that in air oxygen vacancies are the minority charge carrier, accordingly ionic conductivity may be too low to polarize the MIEC volume above the current collector, see also below. When normalizing the ASR of the microelectrode with current collector to the free area we obtain 12.3 Ωcm², which is in accordance with the 13.6 Ωcm² found for the microelectrode without current collector. A good agreement is also found for the area corrected chemical capacitance, 1606 F/cm³ and 1293 F/cm³ for the microelectrodes with and without current collector, respectively. The similarity of the area corrected capacitances indicates a similar polarized volume.

These values of C_{chem} can further be compared to values calculated from defect chemical literature data and Eq. 4. Defect chemical properties of thin films may deviate from those of bulk samples,⁵⁴ but the authors are not aware of any detailed data set describing defect thermodynamics of LSF thin films. Therefore, comparison is made with the accurate bulk defect chemical data of LSF64 given by Kuhn et al.¹⁹ From the defect model of LSF64 (Eqns. 1–3), the correlation between oxygen partial pressure p_{O_2} and nonstoichiometry $(3-\delta)$ can be derived.¹⁹ It reads

$$p_{\text{O}_2} = \frac{1}{16} \left(-\frac{1}{K_{\text{ox}}^{1/2}} \frac{(2\delta - 0.4)(3 - \delta)^{1/2}}{(2\delta + 0.6)\delta^{1/2}} + \left(\frac{1}{K_{\text{ox}}} \frac{(3 - \delta)(2\delta - 0.4)^2}{\delta(2\delta + 0.6)^2} + \frac{K_i}{K_{\text{ox}}} \frac{4(3 - \delta)(1.4 - 2\delta)}{\delta(2\delta + 0.6)} \right)^{1/2} \right)^4 \quad [7]$$

with

$$K_i = \frac{[Fe'_{Fe}][Fe^*_{Fe}]}{[Fe^x_{Fe}]^2} \quad 2Fe^x_{Fe} \rightleftharpoons Fe'_{Fe} + Fe^*_{Fe} \quad [8]$$

and

$$K_{\text{ox}} = \frac{[O^x_O][Fe^*_{Fe}]^2}{p_{\text{O}_2}^{1/2}[Fe^x_{Fe}]^2[V_O^{\bullet\bullet}]} \quad \frac{1}{2}O_2 + 2Fe^x_{Fe} + V_O^{\bullet\bullet} \rightleftharpoons O^x_O + 2Fe^*_{Fe} \quad [9]$$

These equations describe the oxygen nonstoichiometry of bulk LSF64 from 1 bar to the decomposition oxygen partial pressure, measured by thermogravimetry and coulometric titration. Bucher and Sitte used the same defect chemical model to quantify electronic conductivity relaxation experiments of LSF46.^{33,55} In the following, Eq. 4 is applied to estimate chemical capacitances of our LSF64 thin films. K_i and K_{ox} were calculated using the values for standard enthalpy and entropy evaluated by Kuhn et al.¹⁹ Then Eq. 7 was solved numerically for 0.2 bar oxygen partial pressure at 620°C, giving $\delta = 0.0048$. The equilibrium concentration of ionic charge carriers (vacancies) $c_{\text{ion}}^{\text{eq}}$ can be calculated by

$$c_{\text{ion}}^{\text{eq}} = c_0 \cdot \frac{\delta}{3} \quad [10]$$

where $c_0 = 5.07 \times 10^{22} \text{ cm}^{-3}$ is the concentration of oxygen sites in LSF64, determined from the lattice parameters given in 01-082-1961 (ICDD database). For the equilibrium concentration of electronic charge carriers the charge neutrality equation

$$c_h^{\text{eq}} - c_e^{\text{eq}} = (0.4 - 2\delta) \frac{c_0}{3} \quad [11]$$

is used, where 0.4 is the Sr fraction on the A site, c_h^{eq} and c_e^{eq} are hole and electron equilibrium concentrations. We obtain 8.12×10^{19} and $6.60 \times 10^{21} \text{ cm}^{-3}$ for oxygen vacancies and electron holes. A similar estimation of charge carrier density in cerium oxide thin films was

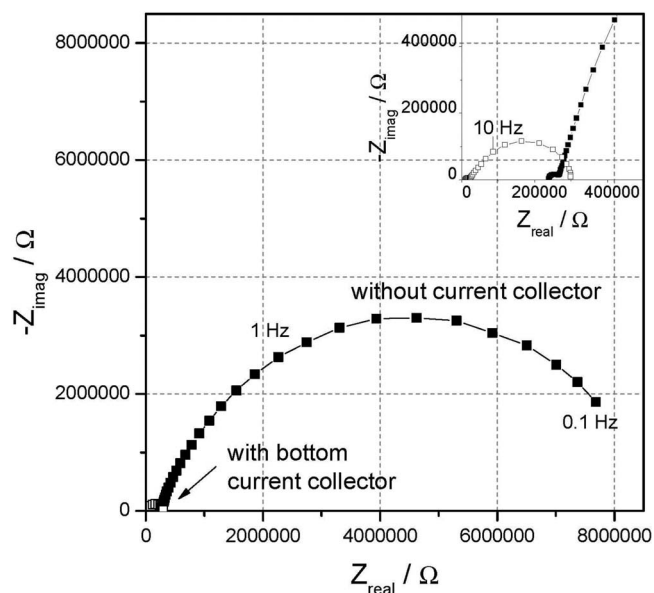


Figure 6. Impedance spectra of LSF64 microelectrodes (95 μm diameter) in humidified hydrogen, with bottom current collector (open squares) and without current collector (filled squares). Both spectra were recorded at 700°C set temperature, T_{calc} for the electrode with current collector is equal to 605°C. For the sample without current collector a meaningful temperature could not be calculated due to the sheet resistance.

conducted by Chueh and Haile.⁴⁹ The calculated concentrations were used in Eq. 4 ($c_{\text{e}on}^{\text{eq}} \approx c_h^{\text{eq}}$) and result in a chemical capacitance at $p\text{O}_2 = 0.2$ bar of 644 F/cm^3 . This value agrees acceptably well with the chemical capacitance found in the measurement, keeping in mind that thermodynamic bulk data rather than thin film data were used in the calculation.

Electrode impedance under reducing conditions.— Importance of current collector.— An impedance spectrum of a circular 95 μm diameter LSF64 microelectrode without additional current collector in reducing conditions is shown in Fig. 6. Compared to oxidizing conditions (Fig. 4), the main arc of the spectrum becomes distorted. However, even more important is the drastic increase of both the size of the electrode-related arc and the high frequency intercept R_a . In principle, two contributions could increase R_a for microelectrodes without current collector. First, a contact resistance between the contact tip and the microelectrode and second, an electronic sheet resistance within the thin film electrode. We exclude the contact resistance between the tip and the sample to be high enough to have an impact on the impedance spectra, also due to its absence in air. The second reason, however, a sheet resistance in LSF64 under reducing conditions, is even expected as LSF64 loses electronic conductivity when changing from oxidizing to reducing conditions, see Introduction. A high sheet resistance reduces the electrochemically active area to the vicinity of the contact tip and thus also increases the YSZ bulk resistance due to geometrical reasons. In contrast, for microelectrodes with additional current collector the value of R_a corresponds to that expected for the ohmic resistance of YSZ at the given temperature and the electrode impedance is drastically reduced (Fig. 6). A similar reduction of the electrochemically active zone of LSF64 without current collecting grid could be visualized by ^{18}O tracer exchange experiments on polarized thin film samples,⁵⁶ where a high cathodic bias lowered the chemical potential of oxygen in LSF64, in analogy to our experiments in $\text{H}_2/\text{H}_2\text{O}$.

In case of the additional bottom current collector, a shoulder in the intermediate frequency range is followed by a ca. 45° slope, see Fig. 6. Such a slope often indicates relevance of a transmission line, e.g. due to a diffusion limited process. As the amount of oxygen vacan-

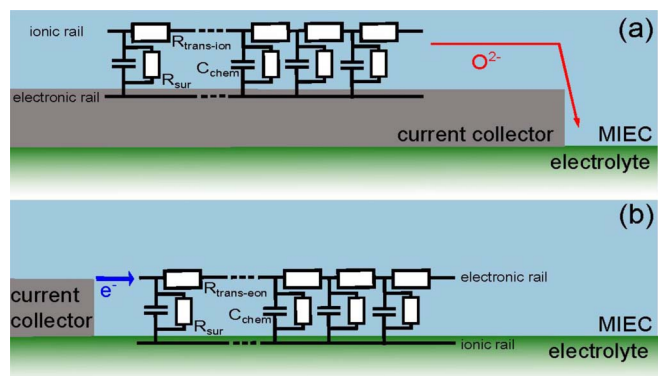


Figure 7. Possible transmission lines describing a MIEC with metallic current collector grid for the case of a) limited lateral ionic conductivity resulting in an ionic transmission line in the MIEC, b) limited electronic conductivity with ionic short circuit in the electrolyte and electronic transmission line. Lateral charge transport lines (given by $R_{\text{trans-ion}}$ or $R_{\text{trans-eon}}$) are set at the correct location (in the MIEC), while the surface resistance R_{sur} has been moved inside the MIEC for reasons of clarity of the equivalent circuit, as R_{sur} and the differential C_{chem} have to be in parallel. However, the actual surface resistance R_{sur} is located at the gas-MIEC interface.

cies in LSF64 under reducing conditions is high, the ionic conductivity is expected to be high. This was also proven by additional ^{18}O tracer experiments using a two step approach for analyzing tracer diffusion under reducing conditions.⁵⁷ Across-plane transport of oxygen can thus hardly cause the 45° feature of a thin film electrode. However, the in-plane transport of oxide ions in LSF64 above the current collecting grid after surface oxygen exchange via $\text{H}_2 + \text{O}^{2-} \rightleftharpoons \text{H}_2\text{O} + 2e^-$ can be modeled by a transmission line circuit (Fig. 7a) which can explain slopes close to 45°. Moreover, the resistive contribution of in-plane electron transport in LSF64 can lead to similar 45° impedance features (Fig. 7b) and of course a combination of both is conceivable, which is discussed in detail in Ref. 38 for $\text{Sr}(\text{Ti},\text{Fe})\text{O}_3$ thin film electrodes.

For the analysis of the chemical capacitance of the sample with current collector, we again used the circuit shown in Fig. 4 and excluded the slope region of the spectrum from the fit. We obtain 103 F/cm^3 , when normalizing to the total LSF64 volume. This is much less than C_{chem} in air and a defect chemical interpretation is possible based on the data reported by Kuhn et al.¹⁹ The corresponding calculation is in analogy to that for oxidizing conditions, with 10^{-23} bar $p\text{O}_2$ at 620°C. This oxygen partial pressure in reducing conditions is estimated from thermodynamic data,⁵⁸ assuming approximately 25 mbar of H_2O in the H_2 2.5%/Ar gas, giving a ratio of $\text{H}_2\text{O}/\text{H}_2$ of 1. Accordingly, the equilibrium concentration of electrons and oxygen vacancies are 2.67×10^{20} and $3.51 \times 10^{21} \text{ cm}^{-3}$, respectively (the hole concentration is $2.00 \times 10^{17} \text{ cm}^{-3}$). This clearly shows that the charge carrier determining C_{chem} is now electronic (electrons) rather than ionic, in contrast to air. From that the chemical capacitance in reducing conditions is calculated to be 545 F/cm^3 . This is within the order of magnitude of the chemical capacitance evaluated from our measurements but the deviation between model and experiment is larger than for C_{chem} in oxygen. This might be caused by differences between defect chemical data of bulk samples and our thin films, but most probably also indicates that not the entire LSF64 film is polarized, due to sheet resistances.

Top vs. bottom current collector under reducing conditions.—The additional current collecting grid influences the electrode impedance differently when it is on top of the LSF64 thin film or buried beneath it (bottom current collector). With top current collector we observe a non-zero high frequency axis intercept (R_a), a small intermediate frequency shoulder and a low frequency arc (R_c , C_c), see Fig. 8. In analogy to oxidizing conditions, the small intermediate frequency feature is assigned to the interfacial resistance and capacitance between electrode and electrolyte. In contrast, for bottom current collector a

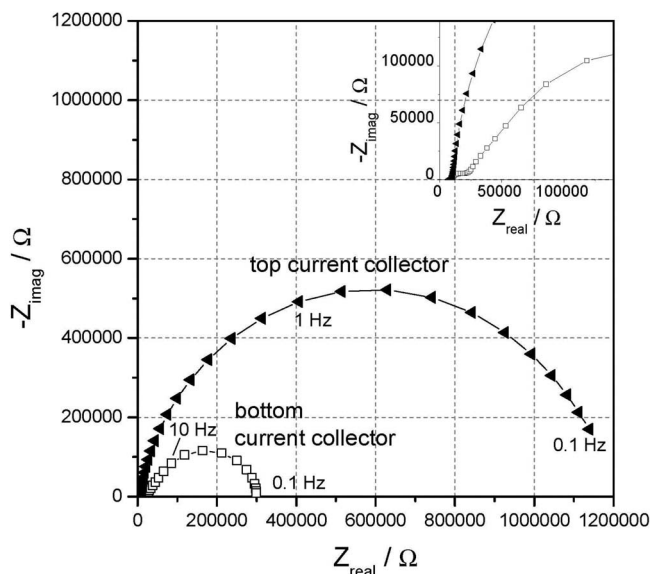


Figure 8. Impedance spectra of LSF64 microelectrodes (95 μm diameter) in humidified hydrogen with top (filled triangles, $T_{\text{calc}} = 623^\circ\text{C}$) and bottom (open squares, $T_{\text{calc}} = 605^\circ\text{C}$) current collector.

pronounced shoulder is found at intermediate frequencies followed by an approximately 45° slope. For the high frequency axis intercept, it does not make a significant difference whether the current collector is beneath or on top of the electrode. The slight difference of R_a in Fig. 8 corresponds to approximately 18°C difference in temperature, which can be caused, for example, by the positioning of the sample on the heating stage or by different mechanical pressures of the contact tip.

In addition to the shape change, the top current collector leads to a substantially larger total electrode resistance, see Fig. 8. This indicates a strongly reduced electrochemically active surface area due to covering approximately 80% of the surface by the current collector, the inactive area is denoted by A3 in Fig. 9b. Areas A1 and A2 in Fig. 9 might be active, but oxygen exchange requires in-plane charge transport of either electrons (A2) or ions (A1). An estimate of this active area (a fraction or even 100% of A1+A2) from the two measured surface resistances in Fig. 8 is difficult since those are prone to statistical variations and also some time-dependent changes (see

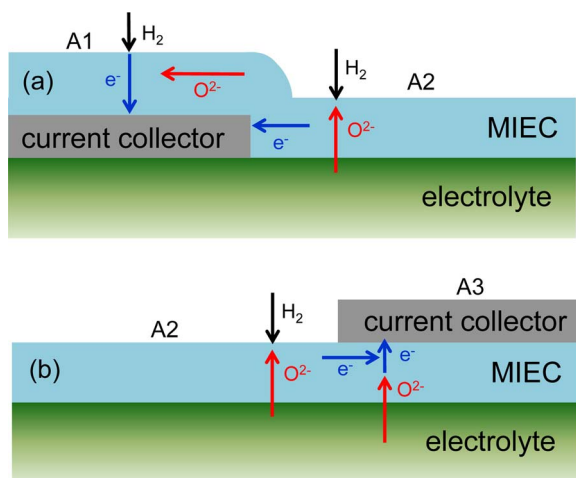


Figure 9. Schematic picture of ionic and electronic current and reaction pathways for bottom (a) and top (b) current collector. A2 represents the free electrode surface area without any current collector beneath or above, while A1 and A3 describe the areas with bottom and top current collector, respectively.

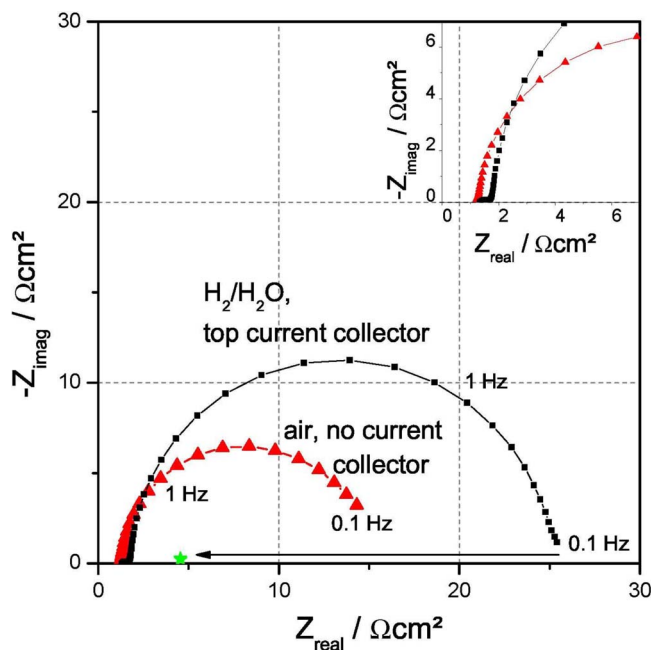


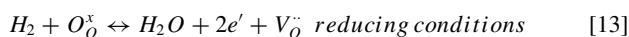
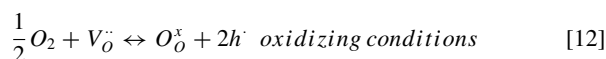
Figure 10. Comparison of impedance spectra of LSF64 microelectrodes (195 μm diameter) in humidified hydrogen with top current collector (black squares, $T_{\text{calc}} = 609^\circ\text{C}$) and in ambient air without current collector (red triangles, $T_{\text{calc}} = 619^\circ\text{C}$). Both spectra are normalized to the total electrode area A_{tot} . The top current collector covers large parts of the surface and the actual surface resistance in reducing conditions normalized to the free surface is therefore $4.5 \Omega\text{cm}^2$ (green star).

Fig. 5). However, additional information can be gained from the chemical capacitance which is very reproducibly measurable. It was determined by using the equivalent circuit in Fig. 4 to fit the low frequency arc. In case of the top current collector, definitely the whole LSF64 volume beneath the metal grid (A3) ($= 0.82 \cdot A_{\text{tot}}$) and possibly large parts of A2 ($= 0.18 \cdot A_{\text{tot}}$) contribute to C_{chem} giving a value of 129 F/cm^3 (normalized to A_{tot}). For the bottom current collector we find 103 F/cm^3 (normalized to A_{tot} , see above). This relatively minor difference clearly shows that a substantial part of the LSF64 surface above a bottom current collector is stoichiometrically polarized and therefore electrochemically active and that considerable lateral ion transport indeed takes place. Activity of A2 only, without polarization of substantial parts of A1, cannot explain the value of 103 F/cm^3 . This is different to oxidizing conditions, see above.

The substantial polarization of LSF64 above the current collector is also in accordance with the very different DC resistances in Fig. 9. A more precise quantification of the fraction of A1 and A2 being active would require fitting by means of transition line models.³⁸ This could then reveal the two decay lengths of the MIEC polarization with increasing distance from the metal grid edge (along A1 and A2). It may also provide further information on the origin of the pronounced shoulder for bottom current collectors. This detailed analysis, however, is beyond the scope of this paper.

Comparison of impedance data in both atmospheres.—So far mainly the effect of a current collecting grid and its influence on the impedance of the LSF64 microelectrodes was discussed. We now compare the impedance of a LSF64 microelectrode without current collector in air and a LSF64 microelectrode with top current collector in reducing conditions (Fig. 10), both 195 μm in diameter. This pair has been chosen since it allows a reasonable comparison of electrode resistances. We already concluded that in air the total electrode surface area is electrochemically active even without a current collector. In reducing conditions the current collector is necessary to compensate the sheet resistance and most probably large parts of the free LSF64 surface (A2 in Fig. 9) are electrochemically active in our case.

As the conductivity of YSZ is essentially independent of the oxygen partial pressure,⁶⁰ the ohmic resistance is expected to be equal at the same temperature. The contribution from the contact resistance is negligible, as mentioned above, and the sheet resistance of the LSF64 in reducing conditions is accounted for by the current collector. The small difference in R_a observed in the spectra is therefore most likely due to the positioning of the sample on the hot stage or different tip pressures, i.e. caused by a slight temperature difference. Calculating the ASR with the total free electrode area (subtracting the area covered by the current collector for the sample in reducing atmosphere) delivers a remarkable result, namely that the very different atmospheres are not reflected in very different resistances. Rather, those are pretty similar: $4.5 \Omega\text{cm}^2$ (green star in Fig. 10) in reducing and $13.6 \Omega\text{cm}^2$ in oxidizing conditions. A part of the remaining difference might even be caused by statistical variations and time dependences of R_c , cf. Fig. 5. This similarity is rather astonishing, taking into account that not only electron, electron hole and vacancy concentration are very different in the two measurements, but even the species participating in the electrochemical reaction are not the same:



An interpretation of this fact cannot be given yet. It might have a very fundamental mechanistic reason but could also be a coincidental result for the given material, gas composition and temperature.

Comparing the chemical capacitances (normalized to A_{tot}) we observe that C_{chem} under oxidizing conditions, where it is proportional to the vacancy concentration (1293 F/cm^3), is approximately one order of magnitude bigger than under reducing conditions, where it is proportional to the concentration of electronic charge carriers (149 F/cm^3 for this specific electrode with top current collector). This indicates that more oxygen vacancies are present in air than electrons in $\text{H}_2/\text{H}_2\text{O}$. A more detailed analysis in terms of the defect chemical model of Ref. 19 was already performed above.

Cyclic change of gaseous atmosphere investigated on macroscopic electrodes.—In order to obtain further information on similarities and differences of LSF64 in oxidizing and reducing conditions, cyclic gas changes were performed on macroscopic $5 \times 5 \text{ mm}^2$ samples with a top current collector (Fig. 3). In the case of these macroscopic thin film electrodes, much less of the electrode area than before is covered by Pt (approximately 20% vs. 80% for microelectrodes). Preparation of working and counter electrodes is described in the Experimental section. The gas flow was changed every two hours from humidified hydrogen to dry synthetic air or back, while the temperature was kept constant at 668°C .

During the gas cycling series impedance spectra were continuously recorded, measuring one spectrum took approximately 12 min. Examples of these spectra are shown in Fig. 11. The shapes of the spectra are similar to those observed for microelectrodes under the respective atmosphere (Figs. 4 and 8). The contribution of the counter electrode to the measured spectra was identified by comparison with impedance spectra from samples with symmetrical porous LSF64/Pt electrodes. A high frequency intercept with a small depressed intermediate frequency arc and a low frequency semicircle is found in oxidizing conditions. Here, the intermediate frequency shoulder could be assigned mainly to the counter electrode rather than to the thin film electrode. Its small additional resistance is within the $R_a + R_b$ part of the equivalent circuit (Fig. 4) and therefore does not influence the analysis of the main working electrode arc at low frequencies.

In reducing conditions, a close to 45° slope of the impedance at intermediate frequencies is followed by two semicircles. In this case, the counter electrode causes the second arc at low frequencies. Its impedance contribution is larger than in air, which is probably due to the increased electronic resistance of LSF64 in reducing atmosphere. Because of the different absolute chemical capacitances of the thin film electrode and the porous counter electrode, the impedance features are

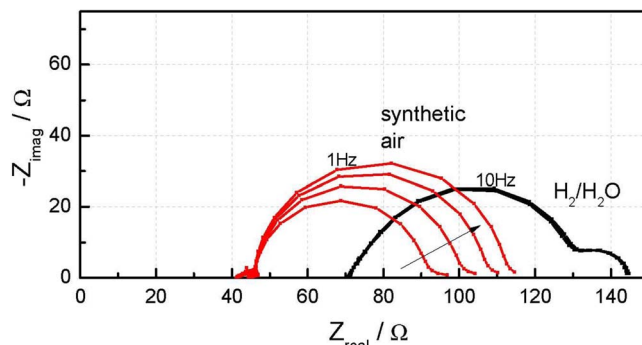


Figure 11. Spectra of samples with macroscopic LSF64 thin film electrodes recorded at 668°C with top current collector and porous LSF64/Pt counter electrode (see Fig. 3) in synthetic air (red) and humidified hydrogen (black). The arrow indicates the change of subsequently measured spectra in synthetic air.

still rather well separated. In reducing conditions, only the main arc was considered in the fit procedure using the circuit of Fig. 4. Due to the overlap of this main arc with the slope at higher frequencies and the counter electrode arc at low frequencies, this fit procedure leads to some inaccuracies, but meaningful comparison of data is still possible.

The high frequency offset under reducing conditions is shifted to higher resistances compared to oxidizing conditions. This indicates different capacitively active areas: In air the electronic sheet resistance of the LSF64 film is low, therefore the parts of the film with substantial distances from the current collectors (see Fig. 3) are still largely involved in the charging and discharging of C_{chem} . Under reducing conditions mainly the area between the fingers and beneath the current collector is reached by the electronic charge carriers. This is confirmed by the numerical analysis of the chemical capacitances. In air C_{chem} has a value of 792 F/cm^3 if normalized to the entire electrode area and this is acceptably close to 1293 F/cm^3 found for microelectrodes without current collector at somewhat lower temperatures.

Normalizing C_{chem} for reducing conditions to the entire area leads to ca. 45 F/cm^3 and thus much less than the values of ca. $100\text{--}150 \text{ F/cm}^3$ found for microelectrodes. However, normalization to the area covered by the current collector plus the area between the fingers, gives very reasonable 90 F/cm^3 . Hence, due to the high sheet resistance the area outside the current collectors is inactive (cf. Fig. 6). Moreover, the macroscopic sample has larger spacing between the current collecting fingers ($23 \mu\text{m}$) than the microelectrodes ($8.5 \mu\text{m}$, see Figs. 2 and 3) and it is likely that the center between the current collecting fingers is only partly polarized. The smaller capacitively active area in reducing conditions causes the larger electrolyte resistance R_a compared to air. However, an exact analysis of this R_a increase would require numerical simulations due to the different active electrode areas on the two sides of the sample (in $\text{H}_2/\text{H}_2\text{O}$).

These considerations also suggest the following normalization of the measured electrode resistances: For the samples in air the electrode resistance is related to the total surface area minus the area covered by the current collector since almost the entire free surface can be assumed to exchange oxygen. For reducing conditions the resistance is related to the area between the metal fingers as this area is assumed to be electrochemically active. The area of a supposedly small active region outside the finger region was neglected. This normalization may slightly overestimate the active surface areas, cf. C_{chem} analysis given above. However, all main messages deduced from the experiments are not affected by this approximation. Fig. 12 shows the change of these normalized electrode resistances R_c with time and gas phase.

First of all, the finding from the microelectrode measurements is confirmed: the area specific electrode resistances in both atmospheres are similar. In the first gas cycle under reducing conditions the ASR is $5 \Omega\text{cm}^2$ and for the first measurement in oxidizing conditions it is approximately the same (Fig. 12). The electrode resistance rises steeply

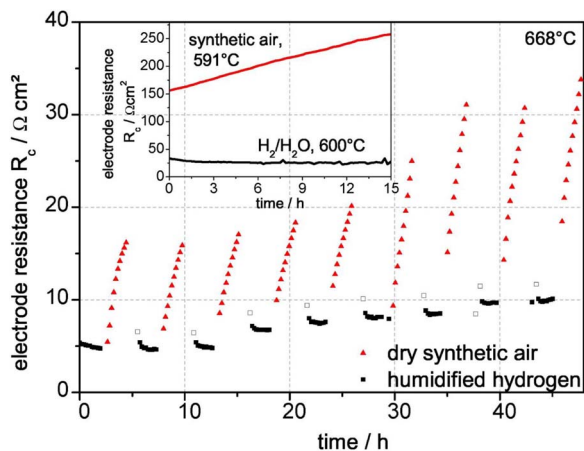


Figure 12. Electrode resistance per area (normalized to the total free LSF surface in oxidizing conditions and the free LSF surface between current collector fingers in reducing atmosphere) over time, at 668°C. Red triangles are measured in synthetic air, while black squares are measured under $\text{H}_2/\text{H}_2\text{O}$. Open symbols indicate that the measurement was taken while the atmosphere in the setup was not yet defined. The inset shows degradation of macroscopic thin film electrodes in the absence of gas cycling in humidified hydrogen (black, $T = 600^\circ\text{C}$) and dry synthetic air (red, $T = 591^\circ\text{C}$).

in dry synthetic air, while its stability under reducing conditions is comparatively high. Stability in $\text{H}_2/\text{H}_2\text{O}$ is in accordance with the fact that the humidified hydrogen used here has an oxygen partial pressure of ca. $1.4 \cdot 10^{-22}$ bar at 668°C which is still in the range where LSF64 is supposed to be stable.¹⁹ Additional measurements on macroscopic electrodes in humidified hydrogen without gas change confirmed the stability, see Fig. 12, inset. The strong changes in air upon gas cycling are in contrast to the high phase stability of the LSF64 bulk material under oxidizing conditions¹⁹ and to the much slower degradation rate observed in the absence of gas cycling (Fig. 12 inset). Degradation in air could be caused by the formation of a less active surface termination or Sr segregation as was found for LSC.^{61,62}

Interestingly, by changing back from oxidizing to reducing conditions the initial electrode resistance is again almost reached. This means that the variation of the electrode resistance under oxidizing conditions is not an irreversible degradation. Rather, exposure to reducing conditions again undoes the strong changes in air. Only on a longer time scale there is a slow degradation of the electrode resistance with time that affects both atmospheres. At present we can only speculate about the mechanisms behind this reversibility of degradation in synthetic air. Possibly, a drastic, but fast chemical/structural reorganization of the LSF64 surface takes place in $\text{H}_2/\text{H}_2\text{O}$, irrespective of the degradation state in air. This might even be the formation of a second phase: Below we present XRD results showing the fast formation of small amounts of Ruddlesden Popper like phases and iron oxides on LSF64 powder samples in $\text{H}_2/\text{H}_2\text{O}$ without decomposition of the main part of the bulk. Also SEM images show additional particles on the surface after (long time) exposure to $\text{H}_2/\text{H}_2\text{O}$, see Fig. 1c. Assuming such a severe change of LSF64 film surfaces in $\text{H}_2/\text{H}_2\text{O}$ would explain the undoing of the degradation in air. This novel surface structure formed in reducing atmosphere seems to be less prone to degradation than the LSF64 surface in air. Also humidity present in $\text{H}_2/\text{H}_2\text{O}$ may play a role here.

In the first cycle, the chemical capacitance is almost one order of magnitude higher in oxidizing conditions than in reducing conditions, in accordance with the findings from the microelectrode measurements. Fig. 13 shows that in air the chemical capacitance is almost constant over the entire measurement, it is not affected by the gas cycling or temporal resistance degradation. The chemical capacitance in reducing atmosphere slowly decreases from ca. 90 to 38 F/cm^3 within 48 hours. This process cannot be reversed by gas change to synthetic air. The chemical capacitance is a bulk property (in contrast

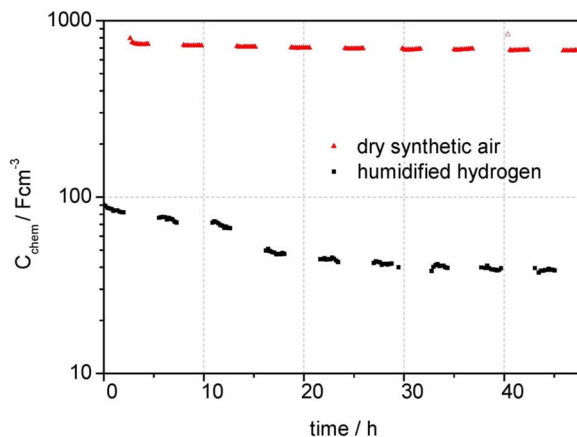


Figure 13. Chemical capacitance per volume (normalized to the total electrode area for oxidizing conditions and to the sum of the areas below the entire Pt current collector and between the current collector fingers in reducing conditions) over time, at 668°C. Red triangles are measured in synthetic air, while black squares are measured under $\text{H}_2/\text{H}_2\text{O}$.

to R_e) and the change indicates a variation on the level of the electronic charge carriers of LSF64 in $\text{H}_2/\text{H}_2\text{O}$. A lower concentration of electrons would decrease C_{chem} and a lower electronic conductivity could also reduce the effective area which contributes to C_{chem} , thus lowering the absolute value of C_{chem} . Interestingly, this change does not significantly affect the oxygen vacancy concentration in air, which can be concluded from the almost constant chemical capacitance in oxidizing conditions. Moreover, comparing Figs. 12 and 13 indicates that the change in the bulk C_{chem} and the slow overall degradation of the surface resistance (R_e) in reducing atmosphere are possibly linked. Accordingly, the change of C_{chem} in $\text{H}_2/\text{H}_2\text{O}$ might be related with a slow phase change or second phase formation affecting both the electronic conductivity in the bulk of our film and the electrochemical surface reaction.

In both graphs (Figs. 11 and 12) data points immediately after gas changes, marked with open symbols, seem to deviate from the general trend. However, from the peak frequencies in the impedance spectra (approximately 0.5 Hz in oxidizing and 10 Hz in reducing conditions, Fig. 11) we can conclude that the equilibration to the different atmospheres is fast. Hence, the deviation is most probably simply due to the slow gas change in the setup which leads to an undefined gas mixture in the first minutes of the measurement.

High-temperature in-situ X-ray diffraction on LSF64 powder.—In-situ high-temperature powder XRD was performed to investigate possible phase changes in reducing conditions. XRD can detect a phase change if sufficient material does undergo the change. A phase change may be restricted to the surface or only occurs to a minor degree, which is why it can be difficult to detect on thin films even with grazing incidence XRD. Therefore we used LSF64 powder through which a constant flow of humidified hydrogen was applied. The powder was exposed to a temperature profile (see Fig. 14 inset) and the measured diffraction patterns were compared to those from the ICDD-database (see Experimental).

Fig. 14 shows the diffraction patterns of LSF64 powder in humidified hydrogen, a zoom of the 20–50° region is provided in Fig. 15. The first diffraction patterns, measured below 200°C, show only the LSF64 peaks. Within the first hours of measurement between 50°C and 600°C the area of the LSF64 peaks increases. Additional peaks appear (at 23.8°, 24.6°, 26.7°, 28.9°, 29.2°, 29.8°, 30.4°; 31.2°, 33.1°, 35.2°, 36.0° and 41.8°), starting from 400°C. These peaks do not vanish upon cooling, but their intensity remains rather low over the entire measurement. The peaks emerging around 550°C at $2\theta = 29.8^\circ$ and 35.2° (Fig. 15, black diamonds) can be assigned to Fe_3O_4 . When heating to temperatures above 700°C these two peaks disappear, while two other peaks (black stars at 36.0° and 41.8°) appear, indicating a

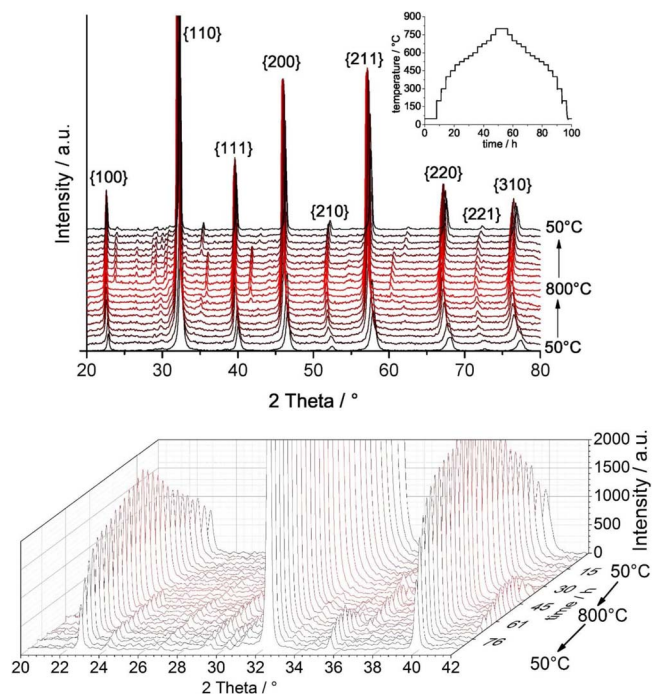


Figure 14. Diffraction pattern (Cu-K α) of LSF64 powder in humidified hydrogen. Top: Reflections of LSF are given with their respective (hkl) indexes. Inset: Temperature profile; at each dwell temperature diffraction patterns were collected. Bottom: 3D plot of measured diffraction patterns with time.

transition from Fe₃O₄ to FeO. The different transition temperatures (Fe₃O₄ to FeO at around 700°C, FeO to Fe₃O₄ at around 550°C) indicate that at least one transition is kinetically hindered. After the formation of the iron oxides, their peaks do not further grow in intensity over the entire measurement. This suggests that an equilibrium is reached after the precipitation of a small amount of iron oxide and large parts of the material do not demix. A comparison of peak areas of the peaks with highest intensity of LSF64 ($2\Theta = 32.2^\circ$) and Fe₃O₄ ($2\Theta = 35.2^\circ$) at 550°C (cooling) indicates the formation of 1.7% magnetite.

Besides the formation of the iron oxides, other peaks arise and remain present even after cooling the powder back to 50°C. The major

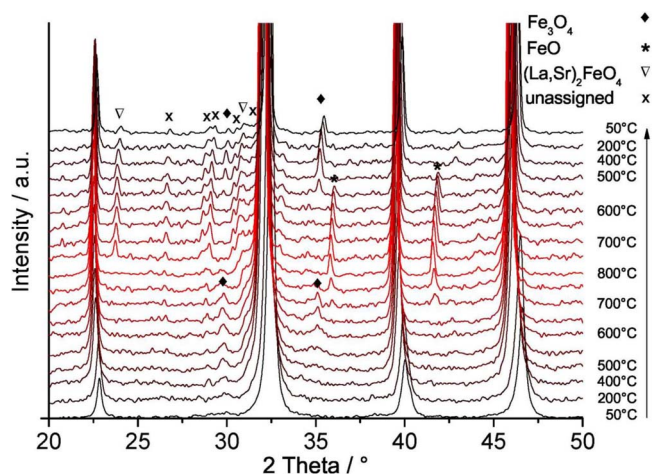


Figure 15. Diffraction pattern (Cu-K α) of LSF64 in humidified hydrogen in the angular range of 20–50°. Peaks due to different crystalline phases are marked as follows: Fe₃O₄ (black diamond), FeO (star), Ruddleston-Popper like phase (La,Sr)FeO₄ (open triangle) and unassigned peaks (x).

peak of a Ruddleston Popper phase is at 31.249° and indeed a shoulder can be seen for the (110) LSF64 peak around 31° which grows with increasing temperature. Furthermore, the peak forming at 23.8° is also assigned to this Ruddleston Popper phase (Fig. 15, open triangle). Other peaks appeared between 25–33°, but could not be assigned. The formation of a Ruddleston Popper like phase is in agreement with the loss of iron from the perovskite phase, i.e. the formation of iron oxide. Ruddleston Popper like phases in strontium ferrites have already been investigated in Refs. 63–65 and the ternary phase diagram of La₂O₃-SrO-Fe₂O₃ in air at 1100°C shows multiple Ruddleston Popper phases.⁶⁶ Further, the loss of iron from the perovskite and the formation of a Ruddleston Popper phase were observed in Refs. 19 and 67. XRD measurements in H₂ (5%)/He²⁶ probably have not shown these secondary phases due to the use of pressed and sintered LSF pellets, where the gas LSF interphase is limited to the pellet surface. Total decomposition of the LSF64 powder was observed in dry hydrogen, which is in accordance with thermogravimetric measurements.¹⁹

In principle the oxygen vacancies could also order to form a Brownmillerite-like phase. Bahteeva et al.²⁶ observed the formation of Brownmillerite-like structures in La_{1-x}Sr_xFeO_{3- δ} for $x > 0.5$ at 700°C in a hydrogen (5%)/helium mixture, they speculated that the oxygen vacancies are randomized in a composition range of $x \leq 0.5$. Still, a Brownmillerite-like phase may form in LSF64 at lower temperatures, where oxygen vacancy ordering is more likely. From the diffraction patterns we cannot confirm the formation of Brownmillerite-like phases in LSF64 as their respective peaks superimpose with those of LSF64 and the Ruddleston-Popper phase. However, the peak found at 33.1° would fit to a Brownmillerite-like phase.

These XRD results indicate that in the temperature range of our thin film studies LSF64 quickly forms small amounts of secondary phases in reducing conditions, despite nominally remaining within the stability limit found in Ref. 19. Irrespective of these phase formations, the main LSF64 peaks remain by far the largest. Possibly, surfaces with their different energetics are already unstable in our reducing atmosphere and demix while the bulk stays perovskite-type.

Transferring this interpretation to our thin film measurements suggests that iron oxide and a Ruddleston Popper like phase might be formed on the electrode surface under reducing conditions. This could also happen for a surface degraded in air and thus might be the origin of the reactivation of the LSF64 surface after exposure to oxidizing conditions, as suggested above. If, for example, degradation in air is caused by segregation of a Sr-rich phase or formation of a Sr-rich surface termination (cf. LSC),^{61,62} the surface phases evolving in H₂/H₂O can repeatedly undo these processes by forming the surface being most stable in the reducing atmosphere.

Conclusions

Impedance measurements of well-defined LSF64 thin film microelectrodes with and without additional current collector could be successfully carried out under oxidizing as well as reducing conditions. The low electronic conductivity of LSF64 thin film electrodes under reducing conditions leads to a high sheet resistance, which can be overcome by the use of an additional current collector. Chemical capacitances (C_{chem}) are about one order of magnitude larger in air, compared to H₂/H₂O and in acceptable agreement with values predicted from defect chemical models in literature. In both cases C_{chem} reflects the concentration of the minority charge carriers, which are oxygen vacancies in air and electrons in H₂/H₂O. The chemical capacitance even allows an estimation of the electrochemically active area and thus determination of area-specific electrode resistances for oxidizing and reducing conditions. Surprisingly similar specific resistances are found in both atmospheres.

These findings were also reproduced with macroscopic LSF64 electrodes that were exposed to a cyclic gas change. Further, the cyclic gas change shows that there is a continuous and severe increase in the electrode resistance under oxidizing conditions after each exposure to reducing conditions. In H₂/H₂O, the previous degradation upon air could be reversed. As a reason we suggest reversible demixing

of near-surface regions in H₂/H₂O with formation of a new stable surface, irrespective of previous surface degradation processes in air. This is in line with high-temperature in-situ XRD measurements, where the formation of small amounts of iron oxides were observed in reducing conditions, together with the formation of another phase which is probably Ruddlesden Popper-like. All together, the results show that LSF64 might be used in SOFC/SOEC electrodes under reducing conditions if prepared with an additional current collector.

Acknowledgments

The XRD measurements were carried out within the X-Ray Center of the Vienna University of Technology. SEM images were recorded at the Universitäre Service-Einrichtung für Transmissionselektronenmikroskopie (USTEM), TU Vienna by Elisabeth Eitenberger. The authors gratefully acknowledge financial support by Austrian Science Foundation (FWF), Projects F4509-N16, P21960-N17, and W1243-N16.

References

- M. A. Laguna-Bercero, *J. Power Sources*, **203**, 4 (2012).
- N. Q. Minh, *J. Am. Ceram. Soc.*, **76**, 563 (1993).
- E. Konyshcheva and J. T. S. Irvine, *ECS Transactions*, **13**, p. 115 (2008).
- T. Nakamura, G. Petzow, and L. J. Gauckler, *Mater. Res. Bull.*, **14**, 649 (1979).
- E. Konyshcheva and J. T. S. Irvine, *Chem. Mater.*, **21**, 1514 (2009).
- E. Lay, G. Gauthier, S. Rosini, C. Savaniu, and J. T. S. Irvine, *Solid State Ionics*, **179**, 1562 (2008).
- S. Tao and J. T. S. Irvine, *Nat. Mater.*, **2**, 320 (2003).
- S. P. Jiang, L. Zhang, and Y. Zhang, *J. Mater. Chem.*, **17**, 2627 (2007).
- I. Jung, D. Lee, S. O. Lee, D. Kim, J. Kim, S.-H. Hyun, and J. Moon, *Ceram. Int.*, **39**, 9753 (2013).
- P. Vernoux, *Solid State Ionics*, **135**, 425 (2000).
- S. Primdahl, J. R. Hansen, L. Grahl-Madsen, and P. H. Larsen, *J. Electrochem. Soc.*, **148**, A74 (2001).
- W. Kobsiriphat, B. D. Madsen, Y. Wang, L. D. Marks, and S. A. Barnett, *Solid State Ionics*, **180**, 257 (2009).
- P. Vernoux, E. Djurado, and M. Guillo, *J. Am. Ceram. Soc.*, **84**, 2289 (2004).
- C. D. Savaniu and J. T. S. Irvine, *Solid State Ionics*, **192**, 491 (2011).
- S. Cho, D. E. Fowler, E. C. Miller, J. Scott Cronin, K. R. Poeppelmeier, and S. A. Barnett, *Energy Environ. Sci.*, **6**, 1850 (2013).
- C. Sun and U. Stimming, *J. Power Sources*, **171**, 247 (2007).
- M. Mosleh, M. Søgaard, and P. V. Hendriksen, *J. Electrochem. Soc.*, **156**, B441 (2009).
- S.-i. Hashimoto, Y. Fukuda, M. Kuhn, K. Sato, K. Yashiro, and J. Mizusaki, *Solid State Ionics*, **181**, 1713 (2010).
- M. Kuhn, S. Hashimoto, K. Sato, K. Yashiro, and J. Mizusaki, *Solid State Ionics*, **195**, 7 (2011).
- P. Plonczak, M. Gazda, B. Kusz, and P. Jasinski, *J. Power Sources*, **181**, 1 (2008).
- J. Mizusaki, M. Yoshihiro, S. Yamauchi, and K. Fueki, *J. Solid State Chem.*, **58**, 257 (1985).
- J. Mizusaki, T. Sasamoto, W. R. Cannon, and H. K. Bowen, *J. Am. Ceram. Soc.*, **66**, 247 (1983).
- M. V. Patrakeev, J. A. Bahteeva, E. B. Mitberg, I. A. Leonidov, V. L. Kozhevnikov, and K. R. Poeppelmeier, *J. Solid State Chem.*, **172**, 219 (2003).
- M. Søgaard, P. Vang Hendriksen, and M. Mogensen, *J. Solid State Chem.*, **180**, 1489 (2007).
- M. V. V. Patrakeev, I. A. Leonidov, V. L. L. Kozhevnikov, and K. R. R. Poeppelmeier, *J. Solid State Chem.*, **178**, 921 (2005).
- J. A. Bahteeva, I. A. Leonidov, M. V. Patrakeev, E. B. Mitberg, V. L. Kozhevnikov, and K. R. Poeppelmeier, *J. Solid State Electrochem.*, **8**, 578 (2004).
- E. V. Bongio, H. Black, F. C. Raszewski, D. Edwards, C. J. McConville, and V. R. W. Amarakoon, *J. Electroceramics*, **14**, 193 (2005).
- M. C. Kim, S. J. Park, H. Haneda, J. Tanaka, and S. Shirasaki, *Solid State Ionics*, **40-41**, 239 (1990).
- J. Mizusaki, M. Yoshihiro, S. Yamauchi, and K. Fueki, *J. Solid State Chem.*, **67**, 1 (1987).
- J. E. ten Elshof, R. Bellur, and A. I. Kingon, *J. Electrochem. Soc.*, **144**, 1060 (1997).
- J. Yoo, A. Verma, S. Wang, and A. J. Jacobson, *J. Electrochem. Soc.*, **152**, A497 (2005).
- S. Adler, X. Chen, and J. Wilson, *J. Catal.*, **245**, 91 (2007).
- E. Bucher and W. Sitte, *Solid State Ionics*, **173**, 23 (2004).
- J. Goodenough and J. Stickler, *Phys. Rev.*, **164**, 768 (1967).
- P. A. Cox, *Transition Metal Oxides: An Introduction to Their Electronic Structure and Properties*, OUP Oxford, 2010, (1992), p. 94.
- W. C. Chueh, Y. Hao, and W. S. M. Jung, and Haile, *Nat. Mater.*, **11**, 155 (2012).
- C. Zhang, M. E. Grass, A. H. McDaniel, S. C. DeCaluwe, F. El Gabaly, Z. Liu, K. F. McCarty, R. L. Farrow, M. A. Linne, Z. Hussain, G. S. Jackson, H. Bluhm, and B. W. Eichhorn, *Nat. Mater.*, **9**, 944 (2010).
- A. Nanning, A. K. Opitz, T. M. Huber, and J. Fleig, *Phys. Chem. Chem. Phys.*, **16**, 22321-22336 (2014).
- C. Chen, D. Chen, W. C. Chueh, and F. Ciucci, *Phys. Chem. Chem. Phys.*, **16**, 11573 (2014).
- G. Walch, A. K. Opitz, S. Kogler, and J. Fleig, *Monatshfte für Chemie - Chem. Mon.*, **145**, 1055 (2014).
- M. P. Pechini and N. Adams, (1967).
- J. Fleig, F. S. Baumann, V. Brichzin, H.-R. Kim, J. Jamnik, G. Cristiani, H.-U. Habermeier, and J. Maier, *Fuel Cells*, **6**, 284 (2006).
- T. M. Huber, A. K. Opitz, M. Kubicek, H. Hutter, and J. Fleig, *Solid State Ionics*, **268**, 82 (2014).
- A. K. Opitz and J. Fleig, *Solid State Ionics*, **181**, 684 (2010).
- F. S. Baumann, J. Fleig, H.-U. Habermeier, and J. Maier, *Solid State Ionics*, **177**, 1071 (2006).
- F. S. Baumann, J. Maier, and J. Fleig, *Solid State Ionics*, **179**, 1198 (2008).
- A. Wedig, M. E. Lynch, R. Merkle, and M. Liu, *ECS Trans.*, **45**, 213 (2012).
- J. Jamnik and J. Maier, *J. Electrochem. Soc.*, **146**, 4183 (1999).
- W. C. Chueh and S. M. Haile, *Phys. Chem. Chem. Phys.*, **11**, 8144 (2009).
- V. F. Lvovich, *Impedance Spectroscopy - Applications to Electrochemical and Dielectric Phenomena*, A John Wiley & Sons, Inc., (1967), p. 39.
- F. S. Baumann, *thesis*, (2006) <http://elib.uni-stuttgart.de/opus/volltexte/2006/2705/>.
- E. Bucher and W. Sitte, *J. Electroceramics*, **13**, 779 (2004).
- E. Bucher, C. Gspan, F. Hofer, and W. Sitte, *Solid State Ionics*, **238**, 15 (2013).
- T. Kawada, J. Suzuki, M. Sase, A. Kaimai, K. Yashiro, Y. Nigara, J. Mizusaki, K. Kawamura, and H. Yugami, *J. Electrochem. Soc.*, **149**, E252 (2002).
- A. K. Opitz, M. Kubicek, S. Huber, T. Huber, G. Holzlechner, H. Hutter, and J. Fleig, *J. Mater. Res.*, **28**, 2085 (2013).
- K. Langer-Hansel, S. Kogler, W. Hetaba, H. Hutter, and J. Fleig, in preparation.
- L. V. Gurvich, V. S. Iorish, V. S. Yungman, and O. V. Dorofeeva, in *CRC Handbook of Chemistry and Physics*, CRC Press (2009).
- V. V. Kharton, F. M. B. Marques, and A. Atkinson, *Solid State Ionics*, **174**, 135 (2004).
- M. Kubicek, Z. Cai, W. Ma, B. Yildiz, H. Hutter, and J. Fleig, *ACS Nano*, **7**, 3276 (2013).
- Z. Cai, M. Kubicek, J. Fleig, and B. Yildiz, *Chem. Mater.*, **24**, 1116 (2012).
- M. Kubicek, A. Limbeck, T. Froömling, H. Hutter, and J. Fleig, *J. Electrochem. Soc.*, **158**, B727 (2011).
- M. V. Patrakeev, I. A. Leonidov, V. L. Kozhevnikov, and V. V. Kharton, *Solid State Sci.*, **6**, 907 (2004).
- L. Mogni, J. Fouletier, F. Prado, and A. Caneiro, *J. Solid State Chem.*, **178**, 2715 (2005).
- B. V. Beznosikov and K. S. Aleksandrov, *Crystallogr. Reports*, **45**, 792 (2000).
- A. Fossdal, M.-A. Einarsrud, and T. Grande, *J. Am. Ceram. Soc.*, **88**, 1988 (2005).
- D. Bayraktar, S. Diethelm, T. Graule, J. Van herle, and P. Holtappels, *J. Electroceramics*, **22**, 55 (2008).
- T. Horita, T. Shimonosono, H. Kishimoto, K. Yamaji, M. E. Brito, and H. Yokokawa, *Solid State Ionics*, **225**, 141 (2012).